J Braz. Soc. Mech. Sci. Eng. (2017) 39:5057–5067
https://doi.org/10.1007/s40430-017-0774-0

TECHNICAL PAPER

A novel approach for the rolling force calculation of cold rolled sheet

W. Peng[1] · J. G. Ding[1] · D. H. Zhang[1] · D. W. Zhao[1]

Received: 1 July 2016 / Accepted: 22 March 2017 / Published online: 4 April 2017

Abstract The rolling force model was the core factor for the control system of the cold rolled sheet, the prediction accuracy affect the final flatness and the strip thickness directly. A novel approach for the rolling force prediction of cold rolled sheet was first proposed based on the plastic mechanics, in which the cylindrical velocity field was used to analyze the metal flow in the deformation region by the upper bound analysis in this paper. The analysis solution of rolling torque, rolling force and stress state coefficient are obtained by minimizing the total power which contain the internal plastic power, frictional power, shear power and tense power. Moreover, the effects of frictional factor, reduction ratio and the tense on the location of neutral point and stress state coefficient are discussed, respectively, and the validity of the proposed model was verified by comparing with the traditional models. The calculation process was programed and applied in the control system of one 1450 mm cold tandem mill successfully, the prediction results was in good agreement with the actual measured ones, and deviation proportion in the range of ±10.0% reached 97.3%, it can meet the requirements of the control system in cold rolling process.

Keywords Cold rolling · Rolling force · Analytical solution · Cylindrical velocity field

Technical Editor: Eduardo Alberto Fancello.

✉ W. Peng
pengwen233@163.com

[1] State Key Laboratory of Rolling and Automation, Northeastern University, Shenyang 110819, China

1 Introduction

As the core factor in the cold rolling process, the accurate prediction of rolling force is necessary for the increasing demands on the high-quality products. Rolling force has a significant influence on the final thickness accuracy and flatness quality of the cold rolled product [1, 2]. It is necessary to establish a high accuracy method to predict the rolling force parameters, but the non-linear nature of the cold rolling, mechanical and material phenomena make the process difficult to formulate and solve.

Until now, many attempts have been proposed to study the metal flow and to predict the required rolling force in cold rolling process. Many existing traditional rolling force models are based on the theoretical works of Karman [3], who developed the basis of rolling theory, and the equilibrium relationship equation in the micro unit was obtained by the differential equation under a certain assumption. Orowan [4] developed the differential equations of calculating unit rolling pressure based on the slab method in another stress distribution assumption. Tselikov [5] found a solution of Karman's differential equation, the influence of the backward and forward tension stresses were taken into consideration, in his assumptions the contact arc was substituted by chord. Another analytical model of rolling force was derived by Bland-Ford [6], who avoided most of the numerical integration in Orowan's theory. On the basis of Bland-Ford's study, Hill [7] gave the general relation between the rolling force and the required energy in the deformation region. In Stone's research [8], the effects of strip tension were considered based on the simplified slab analysis of deformation region, and his results became the most widely used solution of rolling force in the industrial application.

FEM (Finite Element Method) is another way to study complex deformation. Several researchers established different FEM models to analyze cold rolling process, Abdelkhales et al. [9], Nakhoul et al. [10] and Nielsen et al. [11] established viscoplastic models, and Jiang et al. [12], Zhang et al. [13] and Mei et al. [14] proposed rigid-plastic models, LEE et al. [15] and Poursian et al. [16] used the elastic–plastic models to investigate the cold rolling process. But the large computation time and huge memory capacity during calculation are the disadvantages of the FEM model, especially for personal computers [17]. ANN (Artificial Neural Networks) models had also been widely used in the control system due to their unique model structure and the inherent ability of nonlinear simulation, as well as the high degree of adaptive and fault tolerance characteristics. Researchers developed BP method [18], Bayesian method [19], RBF method [20], adaptive neural method [21] and predictive network [22] to predict the cold rolling force, and Gudur et al. [23] proposed a neutral network-assisted finite model for the simulation analysis of cold rolling process. Whereas, for ANN models, the massive training data is necessary for the offline simulation, the data defects reflected for changed rolling status, in which the calculation accuracy was not always guaranteed.

Because of the high speed in obtaining the analytical solution, the upper bound method was widely used in the metal deformation process [24]. Sezek et al. [25] derived dual-stream function velocity field to analyze cold and hot plate rolling, the rigid plastic boundary of the inlet zone and spread function were both assumed in quadratic form, the required optimum rolling force and final shape from the upper bound analysis show good agreement with the experimental results. Sun et al. [26] proposed a hyperbolic sine velocity field to calculate the rolling force, and the ID yield criterion was applied to obtain the internal plastic deformation power, the online measured data was used to verify the validity of his model. An admissible velocity field of non-bonded sandwich rolling process was developed by Haghighat et al. [27], in his study, the rolling force, mean contract pressure and the final thickness of each layer were determined by the upper bound analysis.

In this paper, to obtain the analytical solution of rolling force and stress state coefficient in cold rolling process, the cylindrical velocity field and strain rate fields are proposed, and then analytical solution of rolling force is obtained by minimizing the total power. Meanwhile, the effect of frictional factor, reduction ratio and the backward or forward tense on location of neutral point and stress state coefficient are discussed, respectively. Also, the calculated results obtained by the proposed model are compared with experimental measured data and other researchers' models.

2 Rolling process

The materials starts with initial thickness h_0, and then rolled through a pair of cylindrical work rolls with roll radius R, the thickness is reduced to h_1, as shown in Fig. 1. Three regions (I, II and III) were divided by the cylindrical velocity discontinuity surfaces, S_1 and S_2. The surface S_1 was the surface jointed by the entrance contract point, and the surface S_2 was joined by the cores of the two work rolls, it was not a velocity discontinuity only because the curvature radius of the section was infinite. The axes r, θ, z of cylindrical coordinate system are chosen to describe the deformation zone. The axis z represents the width direction.

To simplify the calculation through the upper bound analysis, the following assumptions are employed [27]: (1) the work roll is rigid materials; (2) the sheet is symmetric on both the materials and the thickness about symmetry axis; (3) the sheets are rigid plastic materials; (4) the deformation of the sheet is plane strain, only because the change in width during was negligible during the cold rolling process; (5) the frictional factor in the surface was constant.

In the mentioned assumptions, the whole sheet was taken as rigid plastic material, the regions I and III were un-deformation regions. But in fact, in regions outside the plastic deformation zone II, the elastic deformation zone exists in regions I and III, from with Jiang's research [28], the contribution of the rolling force in these parts was less than 3% in the total rolling force, so the assumptions of "materials are taken as rigid and moves as rigid bodies" in this study was acceptable.

The region I and III are the un-deformation regions, and in the region II, the connection line of the symmetry

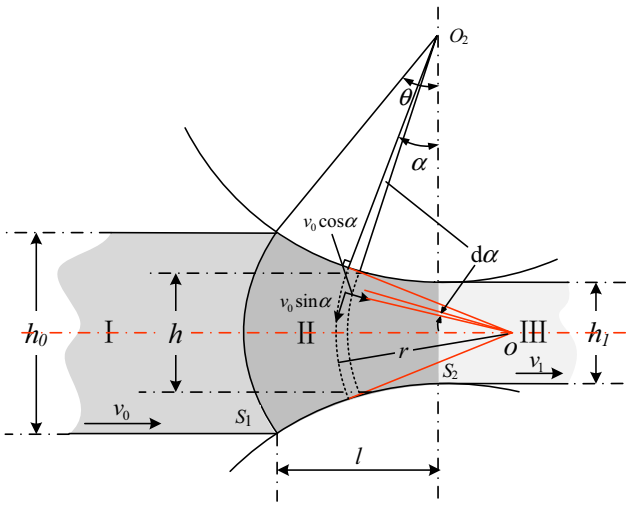

Fig. 1 Definition sketch of the deformation region

points in the upper and down roll were the series of arc with different curvature radius with the origins o. The materials move at speed v_0 before entering the deformation zone, and after rolling it moves at speed v_1. The cylindrical coordinate system with origins o is used to describe the positions of the velocity discontinuity surfaces, contract surface, interface and the velocity components in deformation region.

Thickness in the deformation region with angle α can be expressed as:

$$h_\alpha = h_1 + 2R(1-\cos\alpha) \quad \alpha \in (0,\theta) \tag{1}$$

where α was angle between the surface tangent and the horizontal axis.

The maximum contact angle θ satisfies

$$h_0 = h_1 + 2R(1-\cos\theta), \theta = \arcsin(l/R). \tag{2}$$

3 Upper bound analysis

3.1 Cylindrical velocity field

For cold rolling process, the shape factor of strip was $b/h_m \gg 10$, so the width b can be taken as a constant value, it is assumed that there was no width spread, so the z direction was the non-deforming direction, and $v_z = v_\theta = 0$. Because of the volume constancy, the following relation holds.

$$vh = v_0h_0 = v_1h_1 = v_nh_n = \dot{v}h_n, \tag{3}$$

where h_n was the thickness on the neutral, and the $\dot{v}$ was the circumferential velocity.

From Eq. (1) and (3), the thickness in the neutral surface was:

$$h_n = h_1 + 2R(1-\cos\alpha_n). \tag{4}$$

So the velocity on each connection surface with the angle α can be described as:

$$\begin{cases} v_r = \dfrac{h_1/(2R)+1-\cos(\alpha_n)}{h_1/(2R)+1-\cos(\alpha)}\dot{v} = \dfrac{h_1/(2R)+1-\cos(\alpha_n)}{2\alpha r}\dot{v} \\ v_\theta = 0 \\ v_z = 0 \end{cases}. \tag{5}$$

For the cold rolling process the θ is too small, so the arc length equals to the length of the chord approximately

$$S = 2s = 2\alpha r \approx h = h_1 + 2R[1-\cos(\alpha)]. \tag{6}$$

For the arc in the deformation region, it satisfy the following conditions, the direction of v_r and r are opposite, so the

$$\begin{cases} \dot{\varepsilon}_{rr} = -\dfrac{\partial v_r}{\partial r} = \left[\dfrac{h_1/(2R)+1-\cos(\alpha_n)}{2\alpha r^2}\right]\dot{v} \\ \quad = \dfrac{1}{r}\left[\dfrac{h_1/(2R)+1-\cos(\alpha_n)}{2\alpha r}\right]\dot{v} \\ \quad = \dfrac{2\sin(\alpha)}{S}\left[\dfrac{h_1/(2R)+1-\cos(\alpha_n)}{2\alpha r}\right]\dot{v} \\ \dot{\varepsilon}_{\theta\theta} = \dfrac{v_r}{r} + \dfrac{1}{r}\dfrac{\partial v_\theta}{\partial\theta} \\ \quad = -\dfrac{1}{r}\left[\dfrac{h_1/(2R)+1-\cos(\alpha_n)}{h_1/(2R)+1-\cos(\alpha)}\right]\dot{v} \\ \quad = -\dfrac{2\sin(\alpha)}{S}\left[\dfrac{h_1/(2R)+1-\cos(\alpha_n)}{h_1/(2R)+1-\cos(\alpha)}\right]\dot{v} \\ \dot{\varepsilon}_{r\theta} = \dot{\varepsilon}_{zr} = \dot{\varepsilon}_{\theta z} = \dot{\varepsilon}_{zz} = 0 \end{cases}. \tag{7}$$

Due to $\alpha \le \theta$, $\alpha \le 1$, $\sin\alpha \approx \alpha$, so the velocity in the entry and delivery side were

$$\begin{cases} v_r|_{\alpha=0} = \dfrac{h_1/(2R)+1-\cos(\alpha_n)}{h_1/(2R)} \\ \quad \dot{v} = \dfrac{h_1+2R(1-\cos(\alpha_n))}{h_1}\dot{v} = \dfrac{h_n\dot{v}}{h_1} = v_1 \\ v_r|_{\alpha=\theta} = \dfrac{h_1/(2R)+1-\cos(\alpha_n)}{h_1/(2R)+1-\cos(\theta)} \\ \quad \dot{v} = \dfrac{h_1+2R(1-\cos(\alpha_n))}{h_1+2R(1-\cos(\theta))}\dot{v} = \dfrac{h_n\dot{v}}{h_0} = v_0 \end{cases}. \tag{8}$$

Equations (7) and (8) show that the velocity field expressed in Eq. (5) satisfies the velocity boundary conditions and the geometric equations, so the velocity field is the kinematically admissible velocity and strain rate field.

3.2 Internal plastic deformation power

The internal plastic deformation power is:

$$\begin{aligned} \dot{W}_i &= \frac{2\sigma_s}{\sqrt{3}}\int_V \sqrt{\dot{\varepsilon}_{rr}^2 + \dot{\varepsilon}_{r\theta}^2}\,\mathrm{d}V = \frac{2\sigma_s}{\sqrt{3}}\int_0^\theta \sqrt{2}\dot{\varepsilon}_{rr}RS\mathrm{d}\alpha \\ &= \frac{2\sigma_s\dot{v}h_1}{\sqrt{3}}\left[1+\frac{2R(1-\cos(\alpha_n))}{h_1}\right]\ln\frac{h_0}{h_1}. \end{aligned} \tag{9}$$

3.3 Frictional power

The relative sliding velocity in the contact surface can be expressed as follows:

$$\Delta v_f = v - \dot{v} = \frac{h_1/(2R)+1-\cos(\alpha_n)}{h_1/(2R)+1-\cos(\alpha)}\dot{v} - \dot{v}. \tag{10}$$

The frictional force of the contact surface was $\tau_f = mk$, so the frictional power loss per unit width of sheet along contact surface can be determined as:

$$\begin{aligned}\dot{W}_f &= 2\int_s \tau_f|\Delta v_f|\mathrm{d}s = \frac{2m\sigma_\mathrm{s}}{\sqrt{3}}\int_s|\Delta v_f|\mathrm{d}s \\ &= \frac{2m\sigma_\mathrm{s}}{\sqrt{3}}\left\{\int_0^{\alpha_n}\left[\frac{h_1/(2R)+1-\cos(\alpha_n)}{h_1/(2R)+1-\cos(\alpha)}\dot{v}-\dot{v}\right]R\mathrm{d}\alpha\right. \\ &\left.+\int_{\alpha_n}^{\theta}\left[\dot{v}-\frac{h_1/(2R)+1-\cos(\alpha_n)}{h_1/(2R)+1-\cos(\alpha)}\dot{v}\right]R\mathrm{d}\alpha\right\} \\ &= \frac{2Rm\sigma_\mathrm{s}\dot{v}}{\sqrt{3}}\left\{\frac{b-\cos(\alpha_n)}{\sqrt{b^2-1}}\left[2\arctan\frac{\sqrt{b^2-1}\sin(\alpha_n)}{b\cos(\alpha_n)-1}\right.\right. \\ &\left.\left.-\arctan\frac{\sqrt{b^2-1}\sin(\theta)}{b\cos(\theta)-1}\right]+(\theta-2\alpha_n)\right\} \end{aligned} \tag{11}$$

where $b = h_1/2R + 1$.

3.4 Shear power

There was no shear power loss in exit section, according the geometry relation $\mathrm{d}s = 2R\ \sin\alpha\mathrm{d}\alpha$, $\Delta v_t = v_0\ \sin\alpha$, the equation for the power loss along the shear surface was:

$$\begin{aligned}\dot{W}_s &= \int_s \Delta v_t k\mathrm{d}s = 2Rkv_0\int_s\sin^2\alpha\mathrm{d}\alpha = 4Rkv_0\int_0^{\theta}\sin^2\alpha\mathrm{d}\alpha \\ &= 4Rkv_0\left[\frac{\alpha}{2}-\frac{1}{4}\sin(2\alpha)\right]\Big|_0^{\theta} = 2Rkv_0[\theta-\sin(\theta)\cos(\theta)].\end{aligned} \tag{12}$$

3.5 Tense power

To reduce the rolling force and the power consumption and enhance the flatness quality, the backward tense and forward tense were applied during the rolling process, the tense power can be described as:

$$\begin{aligned}\dot{W}_t &= 4\left(\sigma_\mathrm{b}h_0v_0-\sigma_f h_1v_1\right) = 4\dot{v}h_n\left(\sigma_\mathrm{b}-\sigma_f\right) \\ &= 4\dot{v}[h_1+2R-2R\cos(\alpha_n)]\left(\sigma_\mathrm{b}-\sigma_f\right).\end{aligned} \tag{13}$$

3.6 Total power

Substituting Eq. (9), Eqs. (10)–(13) into the total power function $J^* = \dot{W}_i + \dot{W}_f + \dot{W}_s + \dot{W}_t$, the solution of the total deformation power function can be received according to the first variation principle of rigid plastic material.

Differentiating the total power with respect to the arbitrary variable α_n and making the result set equal to zero, the following equation can be obtained.

$$\frac{\mathrm{d}J^*}{\mathrm{d}\alpha_n} = \frac{\mathrm{d}\dot{W}_i}{\mathrm{d}\alpha_n}+\frac{\mathrm{d}\dot{W}_f}{\mathrm{d}\alpha_n}+\frac{\mathrm{d}\dot{W}_s}{\mathrm{d}\alpha_n}+\frac{\mathrm{d}\dot{W}_t}{\mathrm{d}\alpha_n} = 0, \tag{15}$$

where

$$\begin{cases}\dfrac{\mathrm{d}\dot{W}_i}{\mathrm{d}\alpha_n} = \dfrac{4R\sigma_\mathrm{s}\dot{v}}{\sqrt{3}}\ln\dfrac{h_0}{h_1}\sin(\alpha_n) \\ \dfrac{\mathrm{d}\dot{W}_f}{\mathrm{d}\alpha_n} = \dfrac{2Rm\sigma_\mathrm{s}\dot{v}}{\sqrt{3}}\left\{\dfrac{\sin(\alpha_n)}{\sqrt{b^2-1}}\left[2\arctan\dfrac{\sqrt{b^2-1}\sin(\alpha_n)}{b\cos(\alpha_n)-1}\right.\right. \\ \qquad\left.\left.-\arctan\dfrac{\sqrt{b^2-1}\sin(\theta)}{b\cos(\theta)-1}\right]\right\} \\ \dfrac{\mathrm{d}\dot{W}_s}{\mathrm{d}\alpha_n} = 0 \\ \dfrac{\mathrm{d}\dot{W}_t}{\mathrm{d}\alpha_n} = 8\left(\sigma_\mathrm{b}-\sigma_f\right)R\dot{v}\sin(\alpha_n)\end{cases}.$$

The α_n in different production conditions can be obtained, then the corresponding minimum rolling torque $M_{\min}$, rolling force $P_{\min}$ the stress state coefficient n_σ can be determined, respectively.

$$M_{\min} = \frac{RJ^*_{\min}}{2v_R}, P_{\min} = \frac{M_{\min}}{\lambda\cdot l}, n_\sigma = \frac{P_{\min}}{4\cdot w\cdot l\cdot k}, \tag{16}$$

where λ is the arm factor.

From the solution of Eq. (15), we also obtained the relationship between the frictional factor m and the neutral angle α_n

$$m = \frac{2\sqrt{b^2-1}\left[\ln\frac{h_0}{h_1}+4\sqrt{3}\left(\frac{\sigma_b-\sigma_f}{\sigma_s}\right)\right]}{\arctan\frac{\sqrt{b^2-1}\sin(\theta)}{b\cos(\theta)-1}-2\arctan\frac{\sqrt{b^2-1}\sin(\alpha_n)}{b\cos(\alpha_n)-1}}. \tag{17}$$

4 Results and discussion

A Microsoft Visual Studio program has been implemented to realize the calculation process of the mentioned equations, and the flow chart is given in Fig. 2.

The bite angle was divided into 500 parts, it was small enough to describe the deformation zone, and the increasing step of the reduction ratio was 0.05 and the step of

$$\begin{aligned}J^* &= \dot{W}_i+\dot{W}_f+\dot{W}_s+\dot{W}_t \\ &= \frac{2\sigma_\mathrm{s}\dot{v}h_1}{\sqrt{3}}\left[1+\frac{2R(1-\cos\alpha_n)}{h_1}\right]\ln\frac{h_0}{h_1}+2Rkv_0[\theta-\sin(\theta)\cos(\theta)]+4\dot{v}[h_1+2R-2R\cos(\alpha_n)]\left(\sigma_\mathrm{b}-\sigma_f\right) \\ &+\frac{2Rm\sigma_\mathrm{s}\dot{v}}{\sqrt{3}}\left\{\frac{b-\cos(\alpha_n)}{\sqrt{b^2-1}}\left[2\arctan\frac{\sqrt{b^2-1}\sin(\alpha_n)}{b\cos(\alpha_n)-1}-\arctan\frac{\sqrt{b^2-1}\sin(\theta)}{b\cos(\theta)-1}\right]+(\theta-2\alpha_n)\right\}\end{aligned} \tag{14}$$

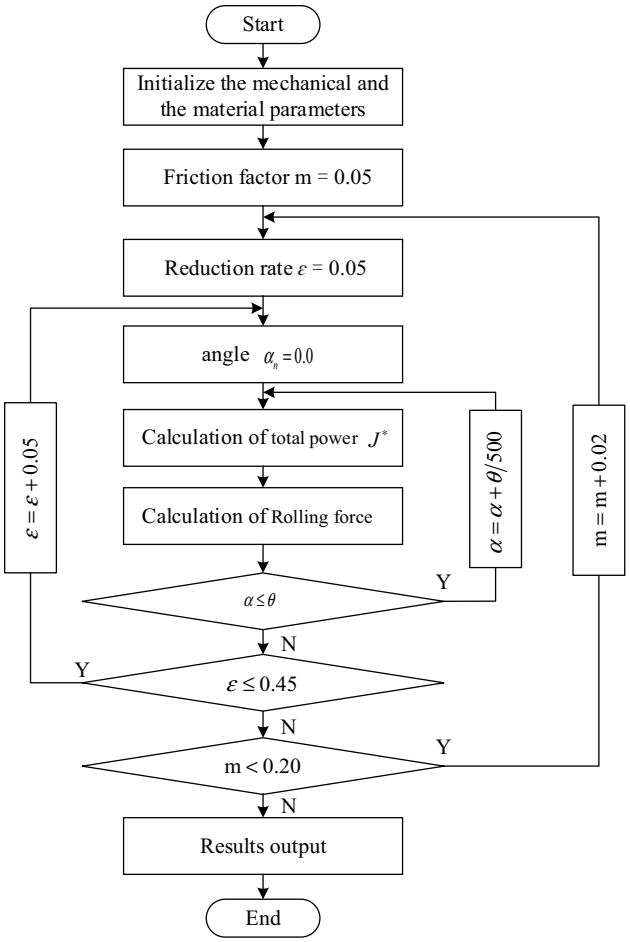

Fig. 2 Flow chart of the calculation process

the frictional factor was 0.02 in the range, both are typically used in simulations.

The mechanical properties and the material parameters were initialized first, then the process of finding the optimal solution was finished with a series of cyclic iterative process, in which the frictional factor, the thickness reduction ratio and initial angle were included, then the required minimal total power, the rolling force and neutral point position were obtained. The following analysis was based on the calculation results.

4.1 Rolling force and power

Figure 3 shows the trend of the total power during the search of the minimum power for different frictional factor. It is shown that for the same frictional factor, the total power changes with the change of neutral angle, also the minimum of total power increases when the frictional factor increases. In other words, the required rolling force increases with increasing of the frictional factor.

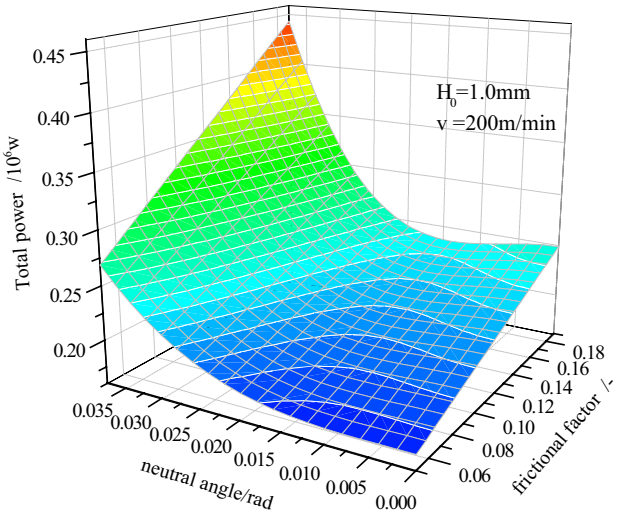

Fig. 3 Variation of total power with the neutral angle change ($\varepsilon = 0.3$)

Figure 4 displays the proportion of each power in total power as the reduction ratio changed ($m = 0.07$). While the backward and forward tense stress are constant, as the reduction ratio increases, the proportion of shear power and the tense power were in a small value, the inter deformation power contributes the main proportion, which was always in a high level, and the proportion of friction power increased as the reduction ratio increasing, because the sheet used in the present paper satisfies $l/h_m \ge 1$.

4.2 Impact of m, ε and σ_b, σ_f on the position of neutral angle

The neutral angle position (described by α_n/θ) is a key parameter in the deformation zone. The following sections

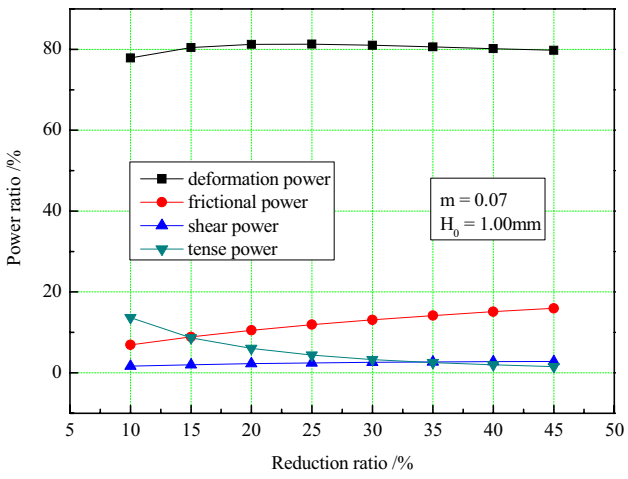

Fig. 4 The proportion of each power in total power as the reduction ratio changed ($m = 0.07$)

show the change of the location of neutral point α_n/θ with the influenced factors (frictional factor m, reduction ratio ε and the tense stress).

Figure 5 shows the location of neutral point α_n/θ is a function of the reduction ratio and the frictional factor, it shows that the neutral point moves toward the exit side when m decreases or ε increases, it means the forward slip decreases as m decreases or ε increases.

Figure 6a, b illustrate the effect of backward and forward tension stresses on the location of neutral point α_n/θ. As the σ_b/σ_s increases, the location of the neutral point moves toward the exit side, also the same trend occurs while σ_f/σ_s decreases. And we also found that, with the increasing of the reduction ratio, the impact of tense on the position of the neutral point was linear approximately.

4.3 Impact of m, ε and σ_b, σ_f on stress state coefficient

The stress state coefficient n_σ is another key factor to describe the rolling status. The following sections show the relationship between the stress state coefficient n_σ and the influenced factors (frictional factor m, reduction ratio ε and the tense stress).

Figure 7 illustrates that stress state coefficient n_σ is a function of the frictional factor m and reduction ratio ε. It can be seen that n_σ increases linearly as ε or m increases. The obtained results are compared to the traditional model as KopoaeB's, Stones, Hill's and Tselikov's results, as shown in Fig. 8, it shows that the stress state coefficient obtained by the proposed model are in a good agreement, the maximum error was less than 6.1%.

Figure 9 shows the impact of the backward and forward tension on the stress state coefficient. It can be seen that n_σ decreases linearly as σ_b/σ_s or σ_f/σ_s increases. Because with the increasing of the backward or forward tension stress, the value of deformation resistance of the strip decreases in a linearly way, which make the rolling force decreases.

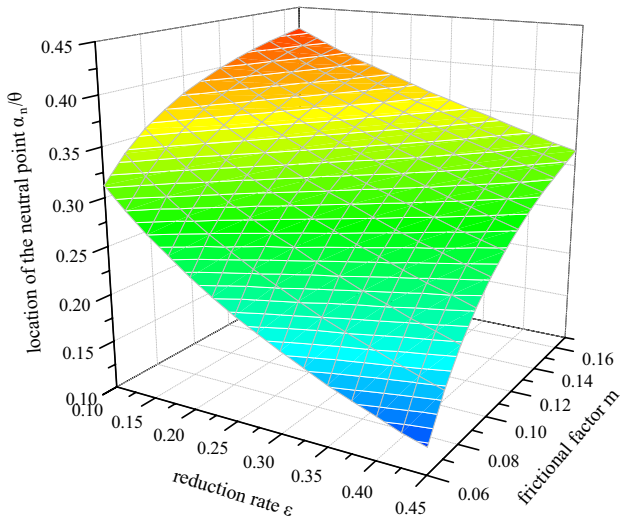

Fig. 5 Effect of frictional factor m and reduction ε on the location of neutral point α_n/θ

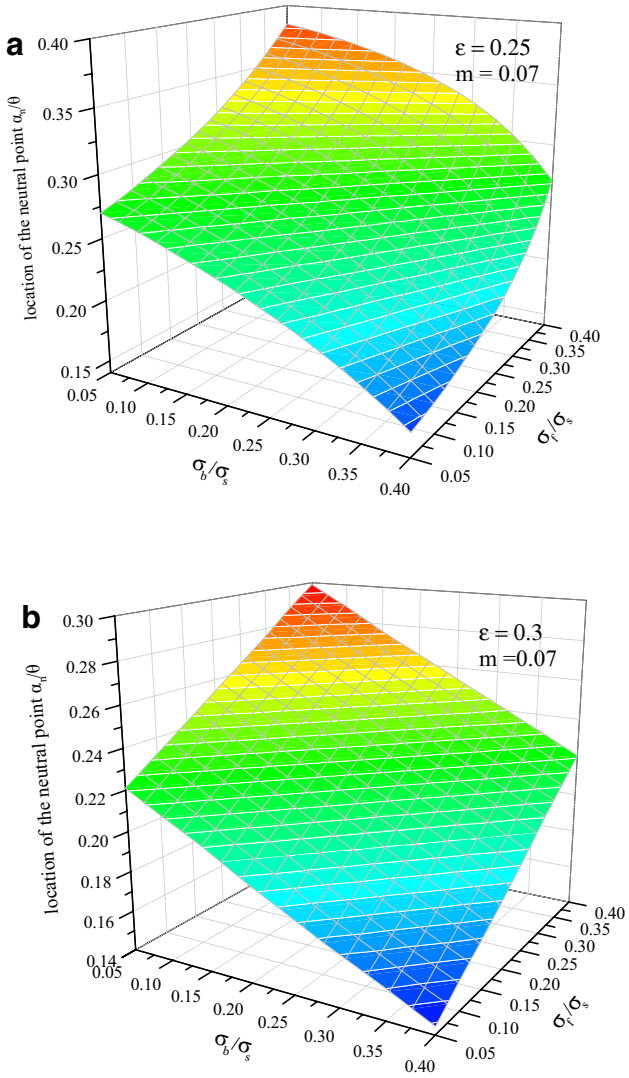

Fig. 6 **a** Effect of tense on the position of the neutral point α_n/θ ($\varepsilon = 0.25$). **b** Effect of tense on the position of the neutral point α_n/θ ($\varepsilon = 0.3$)

5 Application

5.1 Experimental work

To verify the validity of the analytical model proposed in this paper, the results obtained from Eq. (16) are compared with the actual experimental data. A series of experiments has been carried out by an experimental four-high reversing cold mill,as shown in Fig. 10. The experimental

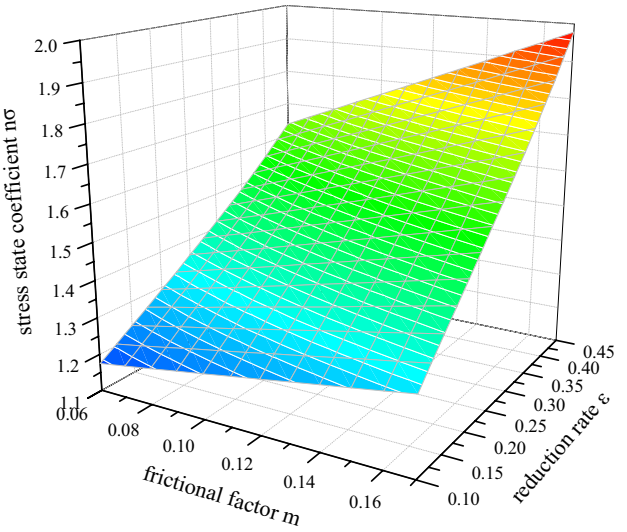

Fig. 7 Effect of frictional factor m and reduction ratio ε on stress state coefficient n_σ

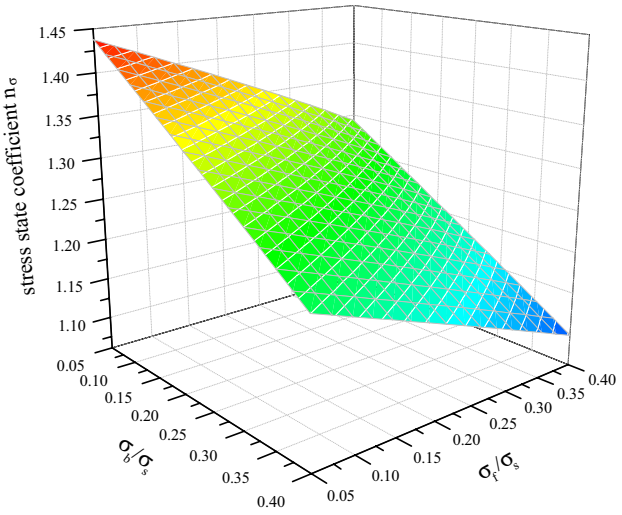

Fig. 9 Effect of tense stress on stress state coefficient n_σ

slabs (initial size: 1.35 mm × 150 mm)rolled through the pair of work rolls (Ø165 mm) with the maximum circumferential velocity in 1200 m/min, the thickness were measured by the thickness gauge in the entrance and delivery sides, the strip speed was measured by the laser speed gauge, and the rolling force were measured by the pressure sensor.

The experimental material used in the experiments is SPCC steel, and the strip is reduced from 1.35 mm to 0.17 mm in five pass. The roll rolling schedule of each pass in shown in Table 1.

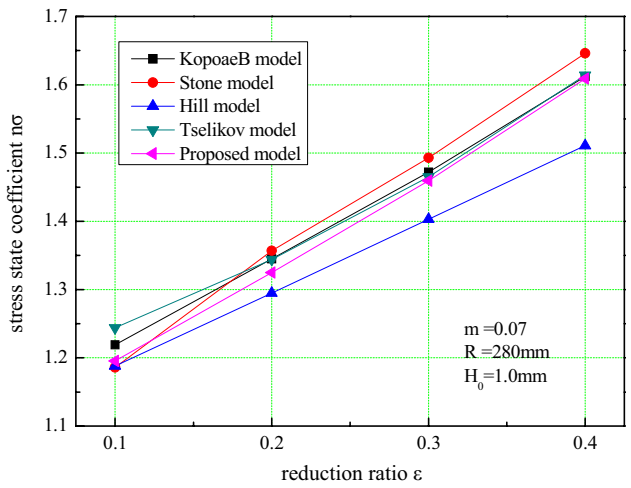

Fig. 8 Compare between the proposed and traditional models in stress state coefficient n_σ

The regression model of deformation resistance for the SPCC was described in Eq. (18), the regression coefficient was shown in Table 2.

$$\sigma = \left(a_0 + a_1\dot{\varepsilon}_{\sum}\right)\left(1 - a_3 e^{a_4\dot{\varepsilon}_{\sum}}\right), \tag{18}$$

where $\dot{\varepsilon}_{\sum}$ was the cumulative reduction ratio, $\dot{\varepsilon}_{\sum} = \frac{1}{3}\left(\frac{H_0-h_0}{H_0}\right) + \frac{2}{3}\left(\frac{H_0-h_1}{H_0}\right)$.

Taking into account the influence of backward and the forward tension, the deformation resistance is expressed further:

$$\sigma_s = \sigma - \left[(1-\beta)\sigma_b + \beta\sigma_f\right], \tag{19}$$

where β was the tense influence coefficient, $\beta = 0.3$ for cold rolling [29].

The sheet rolled in five passes based on the schedule in Tabel 1, and the actual rolling force data was collected and compared with the proposed model and the traditional models(e.g. KopoaeB's, Hill's and Stone's models). All the calculated results was obtained offline.

Figure 11 shows the comparison results of the actual and the predicted rolling force, it can be seen that the proposed model and Hill's models were in a better agreement with the actual ones, and the maximum error was less than 5.2%, meanwhile, the predicted error of KopoaeB's and Stone's result were about 7.0 and 9.3%. The average error and the variance were shown in Table 3, though the average error of the proposed model was higher than Hill's model, the smaller variance showed a better stability.

It should be pointed out that, comparing to Hill's model, the predicted precision in each pass were a little bigger than the actual ones in each pass, that is because the proposed method was based the upper bound method.

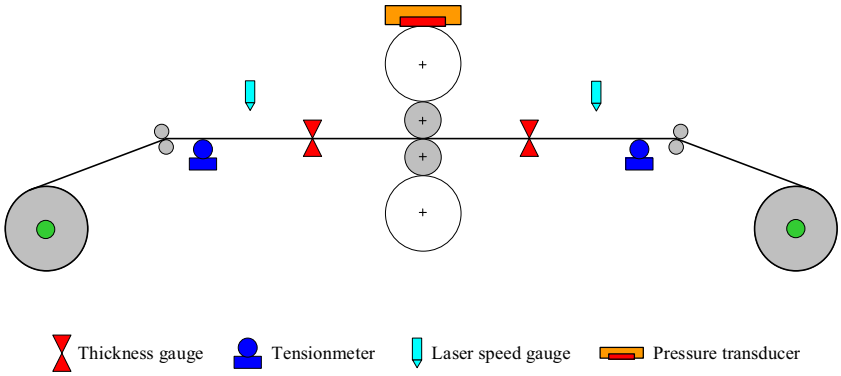

Fig. 10 Structure of experimental four-high reversing cold mill

Table 1 Rolling schedule ($h = 0.17$ mm)

Pass No.	H (mm)	h (mm)	v (m/min)	$\dot{\varepsilon}_{\sum}$ (%)
1	1.350	0.898	200	22.1
2	0.898	0.567	300	49.7
3	0.567	0.361	400	68.1
4	0.361	0.241	400	79.1
5	0.241	0.170	1200	85.7

Table 2 Regression coefficient of the SPCC deformation resistance model

Coefficient	a_1	a_2	a_3	a_4
Value	498.0	136.0	0.2	−5.0

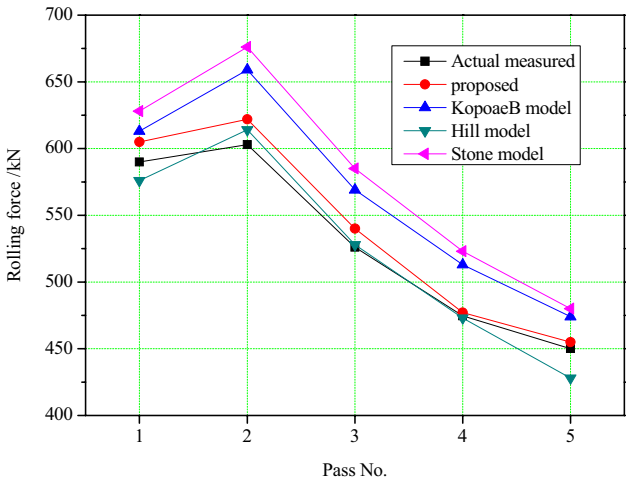

Fig. 11 Comparison of the rolling force between the proposed model actual and measured

Table 3 The statistics of the model error in each pass

Error in each pass	Proposed	KopoaeB	Hill	Stone
1	2.5	3.9	2.5	6.5
2	5.1	9.3	1.8	12.2
3	2.7	8.2	0.5	11.2
4	0.5	8.1	0.3	10.2
5	1.2	5.3	5.3	6.7
Average error/ %	2.4	7.0	2.1	9.3
Variance	1.6	2.0	1.8	2.4

5.2 Industrial work

To check the accuracy of rolling force model, the calculation process has been programed and applied in the control system of one 1450 mm cold tandem mill in a domestic factory of Tangshan. The slabs were reduced from 1.8–4.0 mm to 0.18–0.5 mm, and the diameter of the work roll was 400.0 mm. Figure 12 shows the mill layout and instrument arrangement.

During the rolling process, the roll linear velocity is measured by the velocity sensor, and the thickness is given by the X-ray thickness gauge, the rolling force is given by the pressure sensor located over the bearing blocks of the top work roll, the strips velocity was measured by the laser speed gauge.

The frictional factor used in the experiment from the following equation [30]:

$$m = (m_0 + m_v + m_r)(1 + m_w)(1 + m_\varepsilon), \tag{20}$$

where m_0 is basic value of frictional factor; m_v is speed influence factor of friction; m_r is roughness influence factor of friction, m_w is the wear influence factor of friction; m_ε is the reduction influence factor of friction.

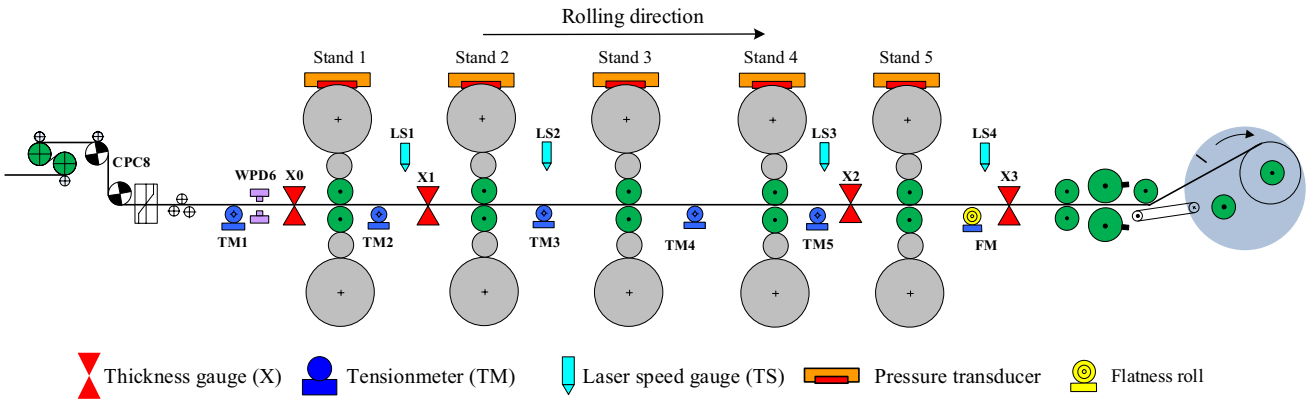

Fig. 12 The 1450 mm cold tandem mill layout and instrument arrangement

The influence of work roll elastic deformation should not be ignored, so the Hitchcock's flattening radius formula [31] should be taken into the consideration in the iteration process in Fig. 2, as:

$$R' = R\left(1 + \frac{16(1-\nu^2)}{\pi E} \cdot \frac{F}{w\Delta h}\right). \tag{21}$$

When the roll radius deviation between two iteration calculations was smaller than the convergence value (less than 0.01%), the iteration finished. The flow chart was shown in Fig. 13.

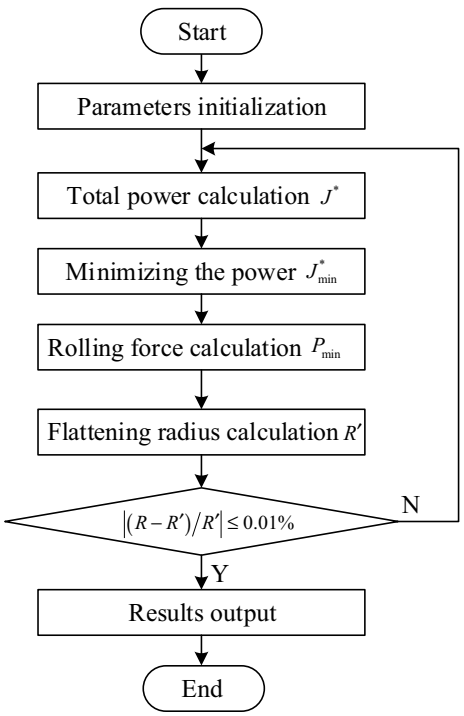

Fig. 13 Flow chart of the iteration process

More than 1500 records were collected, and the comparison between the proposed model and measured ones were shown in Fig. 14.

Compared with the industrial actual data, the rolling force predicted by the proposed model shows a good agreement with the actual measured ones. Also we found that the proportion (predicted results greater than the actual measured ones) is about 60%, that because the method we used to calculate the rolling force was based on the upper bound analysis. The data deviation distribution histogram is given in Fig. 15, data analysis results shows that and the deviation proportion in the range of ±5.0% was 77.2%, the proportion in the range of ±10.0% reached 97.3%, the results shows that the accuracy was high, and the effectiveness of the proposed model was verified further.

The time required for the model calculation was less than 1.0 s; it means that the proposed model meets the requirement of the online control process control system of the cold rolling.

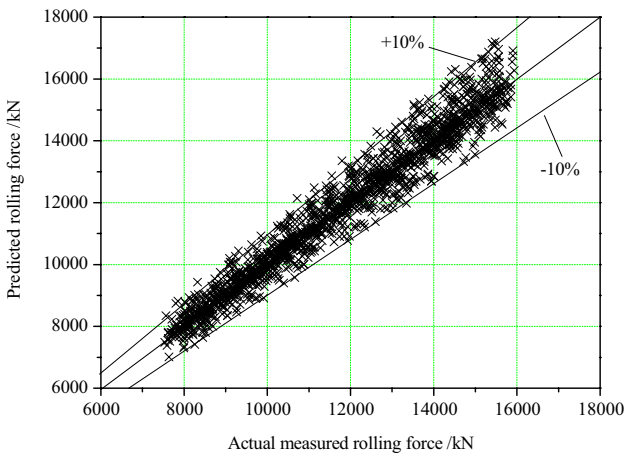

Fig. 14 Comparison rolling force predicted by proposed model with measured results

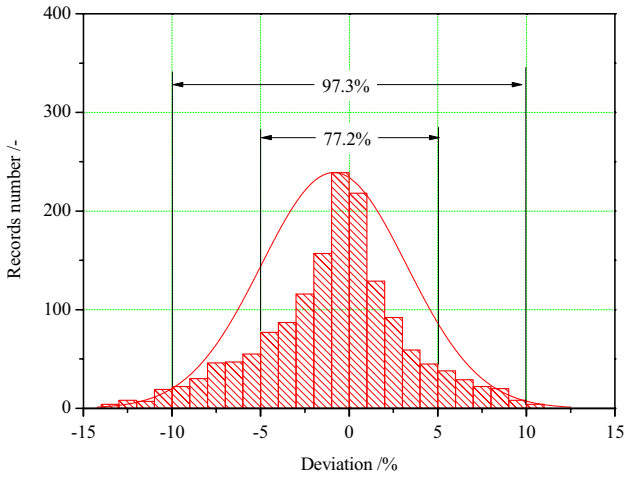

Fig. 15 Deviation distribution histogram

6 Conclusion

1. The cylindrical coordinate velocity field and the corresponding strain rate field are applied to the upper bound analysis of the cold rolling process, and the analytical solutions of rolling force and the stress state coefficient are obtained.
2. The neutral point moves toward the exit side while the σ_b/σ_s or reduction ratio ε increases, also the similar trend occurred while frictional factor m or σ_f/σ_s decreases. The stress state coefficient tension stress n_σ decreases while the σ_b/σ_s or σ_f/σ_s increases, and the opposite trend occurred while frictional factor m and reduction ratio ε increases.
3. The application results from the experimental mill and the industrial plant show that the prediction precision of the proposed model was in a high level, meanwhile, the calculation speed and accuracy can meet the requirement of the process control system of the cold rolled sheet.

Acknowledgements The authors gratefully express their appreciation to National Nature Science Foundation of China (No. 51504061).

References

1. Pittner J, Simaan MA (2011) Tandem cold metal rolling mill control. Springer, London
2. Zárate LE (2005) A method to determinate the thickness control parameters in cold rolling process through predictive model via neural networks. J Braz Soc Mech Sci Eng 27:357–363
3. Karman V (1925) Betragzur theorie des walavorgangs. Zeitschriftfur angewandte mathematik and mechanic 5:139–141
4. Orowan E (1943) The calculation of roll pressure in hot and cold flat rolling. Proc Inst Mech Eng 150:140–167
5. Tselikov AI (1958) Present state of theory of metal pressure upon rolls in longitudinalrolling. Stahl 18:434–441
6. Bland DR, Ford H (1948) The calculation of roll force and torque in cold strip rolling with tensions. Proc Inst Mech Eng 159:144–163
7. Hill R (1950) Relations between roll-force, torque, and the applied tensions in striprolling. Proc Inst Mech Eng 163:135–140
8. Stone MD (1953) Rolling of thin strip. Iron Steel Eng 30:1–15
9. Abdelkhalek S, Montmitonnet P, Legrand N, Buessler P (2011) Coupled approach for flatness prediction in cold rolling of thin strip. Int J Mech Sci 53:661–675
10. Nakhoul R, Montmitonnet P, Legrand N (2014) Manifested flatness defect prediction in cold rolling of thin strips. Int J Mater Form 8:283–292
11. Nielsen KL (2015) Rolling induced size effects in elastic-viscoplastic sheet metals. Eur J Mech A-Solid 53:259–267
12. Jiang ZY, Tieu AK, Zhang XM, Lu C, Sun WH (2003) Finite element simulation of cold rolling of thin strip. J Mater Process Technol 140:542–547
13. Zhang G, Zhang S, Liu J, Zhang H, Li C, Mei R (2009) Initial guess of rigid plastic finite element method in hot strip rolling. J Mater Process Technol 209:1816–1825
14. Mei RB, Li CS, Liu XH (2012) A NR-BFGS method for fast rigid-plastic FEM in strip rolling. Finite Elem Anal Des 61:44–49
15. Lee SH, Song GH, Lee SJ, Kim BM (2011) Study on the improved accuracy of strip profile using numerical formula model in continuous cold rolling with 6-high mill. J Mech Sci Technol 25:2101–2109
16. Poursina M, Rahmatipour M, Mirmohamadi H (2015) A new method for prediction of forward slip in the tandem cold rolling mill. Int J Adv Manuf Technol 78:1827–1835
17. Zhang SH, Zhao DW, Gao CR (2012) The calculation of roll torque and roll separating force for broadside rolling by stream function method. Int J Mech Sci 57:74–78
18. Larkiola J, Myllykoski P, Nylander J, Korhonen AS (1996) Prediction of rolling force in cold rolling by using physical models and neural computing. J Mater Process Technol 60:381–386
19. Liang XG, Jia T, Jiao ZJ, Wang GD, Liu XH (2008) Application of neural network based on bayesian method to rolling force prediction in cold rolling process. J Iron Steel Res 20(10):59–62
20. Zhou FQ, Cao JG, Zhang J, Yin XQ, Jia SH, Zeng W (2006) Prediction model of rolling force for tandem cold rolling mill based on neural networks and mathematical models. J Cent South Univ 37(6):1155–1160
21. Gálvez JM, Zárate Luis E, Helman H (2003) A model-based predictive control scheme for steal rolling mills using neural networks. J Braz Soc Mech Sci Eng 25:85–89
22. Cho S, Cho Y, Yoon S (1997) Reliable roll force prediction in cold mill using multiple neural networks. IEEE T Neutral Network 8(4):874–882
23. Gudur PP, Dixit US (2008) A neural network-assisted finite element analysis of cold flat rolling. Eng Appl Artif Intell 21:43–52
24. Ma GS, Liu YM, Peng W, Yin FC, Ding JG, Zhao DW, Di HS, Zhang DH (2015) A new model for thermo–mechanical coupled analysis of hot rolling. J Braz Soc Mech Sci Eng. doi:10.1007/s40430-015-0390-9
25. Sezek S, Aksakal B, Can Y (2008) Analysis of cold and hot plate rolling using dual stream functions. Mater Des 29:584–596
26. Sun J, Liu YM, Hu YK, Wang QL, Zhang DH, Zhao DW (2016) Application of hyperbolic sine velocity field for the analysis of tandem cold rolling. Int J Mech Sci 108–109:166–173
27. Haghighat H, Sasdati P (2015) An upper bound analysis of rolling process of non-bonded sandwich sheets. Trans Nonferrous Met Soc China 25:1605–1613

28. Jiang ZY, Tieu AK, Lu CA (2004) FEM modelling of the elastic deformation zones in flat rolling. J Mater Process Technol 146:167–174
29. Sun YK (2010) Model and control in hot and cold rolling mill. Metallurgical Industry Press, Beijing
30. Chen SZ, Zhang DH, Sun J, Wang JS, Song J (2012) Online calculation model of rolling force for cold rolling mill based on numerical integration. In: Chinese control and decision conference, pp 3951–3955
31. Ginzburg VB, Ballas R (2000) Fundamentals of flat rolling manufacturing engineering and materials processing. CRC Press, Florida